

Lattice thermal conductivity of half-Heuslers with density functional theory and machine learning: Enhancing predictivity by active sampling with principal component analysis

Rasmus Tranås^a, Ole Martin Løvvik^{b,c}, Oliver Tomic^d, Kristian Berland^a

^a*Department of Mechanical Engineering and Technology Management, Norwegian University of Life Sciences, Drøbakveien 31, Ås, 1432, Ås, Norway*

^b*Centre for Materials Science and Nanotechnology, Department of Physics, University of Oslo, Sem Sælands vei 26, Oslo, 0371, Oslo, Norway*

^c*Materials Physics, SINTEF, Forskningsveien 1, Oslo, 0373, Oslo, Norway*

^d*Department of Data Science, Norwegian University of Life Sciences, Drøbakveien 31, Ås, 1432, Ås, Norway*

Abstract

Low lattice thermal conductivity is essential for high thermoelectric performance of a material. Lattice thermal conductivity is often computed using density functional theory (DFT), typically at a high computational cost. Training machine learning models to predict lattice thermal conductivity could offer an effective procedure to identify low lattice thermal conductivity compounds. However, in doing so, we must face the fact that such compounds can be quite rare and distinct from those in a typical training set. This distinctness can be problematic as standard machine learning methods are inaccurate when predicting properties of compounds with features differing significantly from those in the training set. By computing the lattice thermal conductivity of 122 half-Heusler compounds, using the temperature-dependent effective potential method, we generate a data set to explore this issue. We first show how random forest regression can fail to identify low lattice thermal conductivity compounds with random selection of training data. Next, we show how active selection of training data using feature and principal component analysis can be used to improve model performance and the ability to identify low lattice thermal conductivity compounds. Lastly, we find that active learning without the use of DFT-based features can be viable as a quicker way of selecting samples.

1. Introduction

With their ability to convert heat to electricity, thermoelectrics find use in several niche technologies ranging from wine coolers, hiking stoves with mobile phone chargers, and radioisotope thermoelectric (TE) generators used to power e.g. the *Curiosity* Mars rover. Thermoelectrics could also contribute to reducing global greenhouse gas emissions through waste heat recovery, but their role is currently limited by the modest efficacy realized in devices [1, 2]. Another limitation is the fact that several state-of-the-art TE materials contain toxic or rare elements [3, 4]. Finding new TE materials has therefore gathered much scientific interest in recent years [5].

The efficiency of TE materials is conventionally given by the dimensionless figure of merit, which is expressed as $ZT = \sigma S^2 T / (\kappa_e + \kappa_\ell)$, where σ is the electrical conductivity, S is the Seebeck coefficient, T is the absolute temperature, κ_e is the electronic thermal conductivity, and κ_ℓ is the lattice thermal conductivity. High ZT requires both a high power factor, $\mathcal{P} = \sigma S^2$, and low total thermal conductivity. In non-metals, κ_ℓ is typically much larger than κ_e , but in heavily doped semiconductors, κ_ℓ and κ_e can be more comparable in size [6, 7]; nonetheless, a low κ_ℓ is still typically needed for achieving high ZT .

High-throughput screening based on first-principle calculations have in recent years been much used in the search for new TE materials [8–14]. Many studies focus on electronic properties and use simple models or estimates of κ_ℓ . One reason for this is that computing κ_ℓ comes at a significant computational cost. The cost arises because accounting for the phonon-phonon interactions due to the anharmonicity of the lattice vibrations requires obtaining third-order force constants extracted from a large number of supercell-based density functional theory (DFT) calculations [15–17]. For this reason, machine learning (ML) methods are increasingly supplementing first-principles based calculations for predicting κ_ℓ [18–25]. Pre-trained ML models can in turn also be made available in convenient web-based applications [26].

The half-Heusler (HH) compounds are a class of cubic compounds with three atoms in the primitive

cell, belonging to the $F\bar{4}3m$ spacegroup. As shown in Fig. 1, the XZ sublattice forms a rocksalt structure, while the YZ sublattice forms a zinc-blende structure [27–29]. Several HH compounds have a high power factor in combination with relatively low κ_ℓ , making HHs attractive for TE applications [8, 13, 30–36]. Recently, Feng et al. [37] used DFT-based calculations to show that the four HH compounds: CdPNa, BaBiK, LaRhTe, and LaPtSb have very low κ_ℓ . LaPtSb and BaBiK also have promising electronic transport properties in addition to low κ_ℓ and could have a ZT competitive with top performing TE materials [38–40]. Because κ_ℓ of these four compounds is much lower than for typical HHs, the set of HH compounds presents itself as a dataset well suited for investigating ML methods to separate low and high κ_ℓ compounds. The high symmetry of HHs also reduces the computational cost of calculating κ_ℓ compared to more complex systems such as layered compounds and compounds with distorted symmetries [41–43]. The reduced cost allows us to generate both training and test sets for assessing κ_ℓ .

Our study is based on 122 HH compounds for which κ_ℓ is computed explicitly using DFT. The compounds are based on a combination of dynamically stable HHs, 54 from groups 4-9-15 (Ti,Zr,Hf)(Co,Rh,Ir)(As,Sb,Bi), 4-10-14 (Ti,Zr,Hf)(Ni,Pd,Pt)(Ge,Sn,Pb), and 48 HHs from groups 5-8-15 (V,Nb,Ta)(Fe,Ru,Os)(As,Sb,Bi) and 5-9-14 (V,Nb,Ta)(Co,Rh,Ir)(Ge,Sn,Pb). The last 20 HHs are the remaining stable compounds studied by

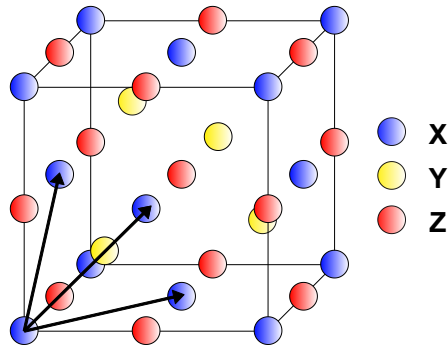


Fig. 1: The HH crystal structure, displayed as the unit cell. The primitive cell is made from the three atoms X , Y , and Z .

Feng et al. [37], based on a revision of the 75 stable HHs identified by Carrete et al. [18].

2. Methods

2.1. Lattice thermal conductivity

DFT calculations in this work are done with the VASP [44–46] software package using the Perdew-Burke-Ernzerhof (PBE) generalized gradient approximation for solids, PBEsol [47, 48]. The plane-wave energy cutoff is set to 600 eV. For relaxations, we use an $11 \times 11 \times 11$ \mathbf{k} -point sampling of the Brillouin zone. The electronic self-consistent loop is iterated until the energy difference falls below 10^{-6} eV, while ionic positions are relaxed until forces fall below 1 meV/Å. The lattice thermal conductivity, κ_ℓ , is calculated with the temperature-dependent effective potential (TDEP) method [16, 49], taking into account three-phonon and isotope-phonon scattering [50, 51]. Fifty configurations based on $3 \times 3 \times 3$ repetitions of the primitive cell are used to obtain second- and third-order force constants. The atomic configurations are taken from a fixed-temperature canonical ensemble at 300 K, where the zero-point motion of the phonons is matched with the Debye temperature [52]. The Debye temperature is obtained from the Voigt approximation of the bulk and shear moduli [53]. A $3 \times 3 \times 3$ \mathbf{k} -point grid is used for the supercell DFT force calculations. We employ a cutoff for second-order pair-interactions of 7 Å while for third-order pair-interactions, the cutoff is set slightly larger than half the width of the supercell (i.e. 6.1 Å for NbCoGe). For the calculation of κ_ℓ , the reciprocal space is discretized on a $35 \times 35 \times 35$ \mathbf{q} -point grid. In a convergence study for NbCoGe, we find these cutoffs to give a numerical error of κ_ℓ less than 3 %.

2.2. Machine learning model

Random forest (RF) regression is a non-linear ML method used in industry and academia alike [54]. An ensemble of decision trees forms the RF model, where each tree is trained on a subset of randomly chosen features and training samples. This randomness makes RF less prone to overfitting. RF has been

shown to perform well in earlier ML studies involving the lattice thermal conductivity [23]. In the RF regression, a given input sample is sorted in each of the decision trees based on its features, so that in a given tree, the sample is assigned to a $\kappa_\ell^{\{i..\}}$ in the training set. Finally, the predicted outcome is given by the mean $\langle \kappa_\ell^{\{i..\}} \rangle$ of the predictions of the ensemble of decision trees.

In ML, failing to identify key features can result in overfitting and reduce method interpretability [55, 56]. Feature selection is here performed using exhaustive feature selection (EFS) in combination with RF regression. EFS assesses the predictive performance of every subset of extracted features and finds the features that give the best outcome of a chosen performance metric. We here choose to use Spearman rank correlation as the metric with five-fold cross-validation, as this correlation measures the predicted ranking of compounds. This brute-force approach carries a significant computational cost, but with the limited number of features in our study, this cost is small compared to that of computing κ_ℓ . EFS is done with the MLXTEND [57] code, while RF regression is done using SCIKIT-LEARN [58]. In the RF model, the hyperparameters of each set of features are optimized using a hyperparameter grid search.

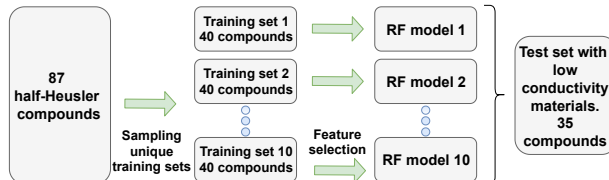


Fig. 2: Flowchart for building the baseline model.

Fig. 2 shows a flowchart for the baseline model. In the model, 87 of the 122 compounds are semi-randomly selected as the training pool for ML, while 35 are left out to provide a test set for model assessment. By semi-randomly, we refer to the fact the five lowest κ_ℓ compounds are in the test set. We make this choice to emulate a not too improbable scenario that could easily arise for larger material classes when only modest-size training sets are used. From the training pool, 10 unique training sets of 40 compounds are se-

lected randomly. The models are retrained based on the features obtained with EFS for final model evaluation. Our baseline model predictions are given by the average of the predictions of these 10 RF models.

In the active sampling scheme, we use principal component analysis (PCA) with the HOGGORM [59] package to identify compounds possessing combinations of feature values that are distinct from those in the training pool. PCA accounts for correlations between features by constructing orthogonal principal components (PC) as linear combinations of feature vectors in feature space. The PCs are oriented in the direction of maximum variance and the features are centered and scaled to unit variance. The PCA analysis is based on all compounds in the study. Using PCA, we identify three compounds, BaBiK, CdPNa, and LaPtSb, that are needed to cover the feature space mapped out by the first two PCs. These three are subsequently included in the training sets from the baseline model, such that the 10 training sets for the active sampling model contain 43 compounds that are used with RF and EFS.

Our study is based on 14 features: 9 are tabulated while 5 are obtained from lost-cost DFT calculations. Two of these, the volume of the relaxed primitive unit cell, V , and corresponding mass density, ρ , could in principle have been obtained from typical tabulated data, standard experiment, or in the absence of such data, from ML models [60–62]. The tabulated features together with V and ρ are grouped as the easily available tier-0 features. Tabulated features are as follows: the ratio between the lightest and heaviest atoms in the primitive cell [63], m_r , the average atomic mass, m_a , the standard deviation of the atomic masses, $m_s = 1/3 \left(\sum_{i=X,Y,Z} (m_i - m_a)^2 \right)^{1/2}$, as well as corresponding features for the electronegativity [64], χ , and covalent atomic radius [65], r . The remaining three, which together with the tier-0 features constitute the tier-1 features, are the lattice thermal conductivity in the Slack model [66], κ_s , the Debye temperature, θ_D , and the bulk modulus, B . These three are related to the elastic tensor [67], and are hence the most time-consuming features to generate. Sections 4.1 through 4.3 are based on tier-1 features, while

Section 4.4 compares the ML performance of models based on tier-0 and tier-1 features.

Higher-order features beyond what we consider, such as the three-phonon scattering phase space, effective spring constants, and first moment frequencies from the phonon density of states [18, 37, 68], can improve the predictions of the ML model, but we here limit ourselves to features that are based on properties that one can expect to be continuously added in material databases such as the MATERIALSPROJECT [69]. Therefore, using such simple features supports a methodology that can later be adopted for screening of larger material databases.

3. Results: Density functional theory calculations

3.1. Lattice thermal conductivity of half-Heusler compounds

Fig. 3 shows the lattice thermal conductivity calculated with TDEP, $\kappa_\ell^{\text{TDEP}}$, at 300 K, 500 K, and 700 K for the 122 HHs. Appendix A: Table A.1 reports $\kappa_\ell^{\text{TDEP}}$ at 500 K. At 500 K, the span of $\kappa_\ell^{\text{TDEP}}$ goes from 0.85 W/mK (LaPtSb) to 23.45 W/mK (LiBSi). Compounds with heavy atoms on the X- or Z-site, such as La, Ba, Bi, and Pb, or with high average mass, typically have lower $\kappa_\ell^{\text{TDEP}}$. The correlation between lattice thermal conductivity and the average mass has been observed for experimental lattice thermal conductivity with compounds across different spacegroups [20]. The ordering of the five lowest $\kappa_\ell^{\text{TDEP}}$ materials from low to high $\kappa_\ell^{\text{TDEP}}$ is consistent with the findings of Feng et al. [37]. The Vanadium-containing compounds VRuBi, VFeBi, VIrPb, VOsBi, VRhPb, and VCoPb have negative phonon frequencies and are not studied further. The two latter have previously been predicted to decompose into elemental phases [70].

In the following, the ML models are based on $\kappa_\ell^{\text{TDEP}}$ at 500 K, which also indicates low lattice thermal conductivity at 300 K and 700 K.

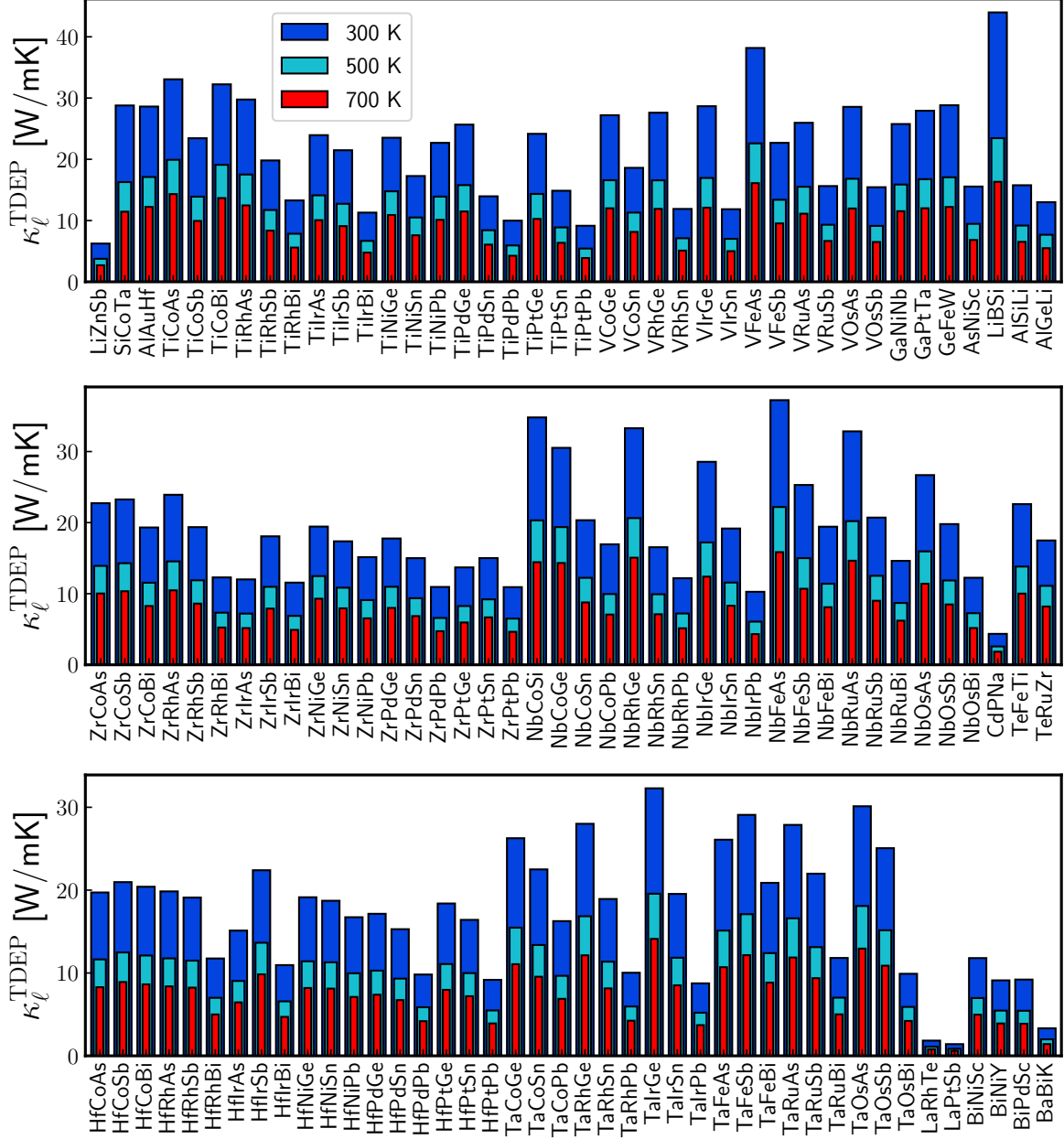


Fig. 3: $\kappa_{\ell}^{\text{TDEP}}$ for the HHs at 300 K (blue bars), 500 K (turquoise bars), and 700 K (red bars).

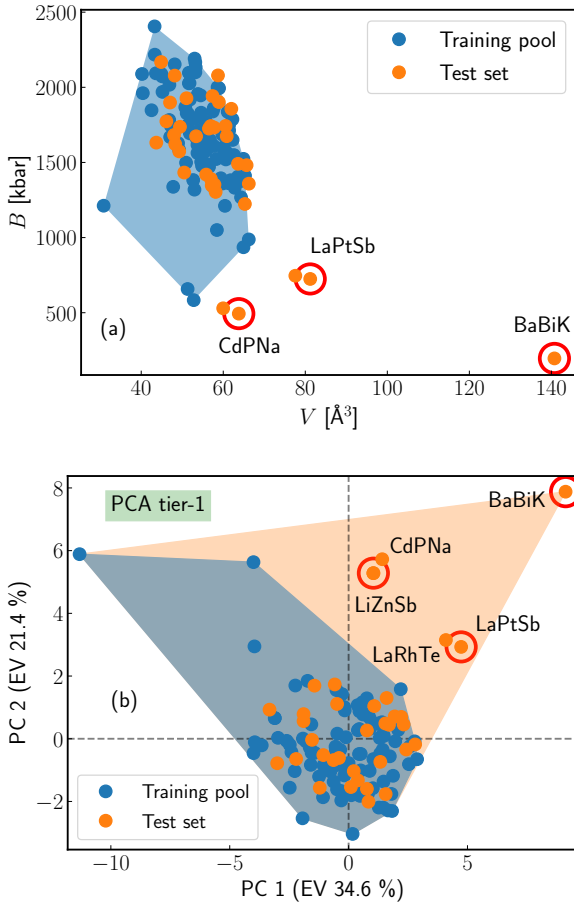


Fig. 4: (a) Scatter plot for the compounds, with V on the horizontal axis and B on the vertical axis. (b) PCA plot for the compounds using tier-1 features. The first PC is shown on the horizontal axis and the second is on the vertical axis. The blue convex hull is the area of the PC space spanned by the 87 materials in the training pool, while the orange convex hull is the area spanned with inclusion of the test compounds.

4. Results and discussion: Machine learning

4.1. Using principal component analysis for diversifying training sets

Fig. 4 (a) shows the position of the compounds in the space spanned by V and B , two features which are known to correlate with the lattice thermal conductivity [18, 20, 71]. In general, low V materials

tend to have less compressed acoustical phonon band structures, increasing the phonon group velocity [72] and thus also the lattice thermal conductivity. Higher B can also be related to stiffer atomic bonds and increased phonon velocities. This is reflected in a Spearman correlation of -0.69 between $\kappa_{\ell}^{\text{TDEP}}$ and V and 0.58 between $\kappa_{\ell}^{\text{TDEP}}$ and B for the compounds in the training pool. The plot shows that some of the compounds in the test set fall outside the convex hull spanned by V and B of the compounds in the training pool. Including such outliers in the training sets, could result in more accurate ML predictions. However, as B and V also have a Spearman correlation of -0.51 , —i.e. higher V tend to relate to less stiff bonds and thus lower B — solely relying on these two features could risk missing important compounds and correlations. This motivates the use of PCA, which offers a more systematic procedure to take all features and their correlations into consideration.

Fig. 4 (b) indicates the position of the compounds of the test set and training pool in the subspace spanned by the two first PCs. This subspace accounts for 56.0 % of the cumulative explained variance (EV) of the feature space. Mapping these two features back to the original feature space, we find the cumulative explained variances of V and B to be 78.6 % and 77.2 %. A comparison of the two convex hulls shows that the low κ_{ℓ} compounds lie outside of convex hull spanned by the training pool.

While PCA can support a human-guided selection of training sets, we choose to formalize this in a systematic procedure that is better suited for automation of the active sampling. The specific compounds to be included are determined iteratively by identifying the compound in the test set with the largest Euclidean distance in the PC space to the closest compound in the current training pool until a marked drop in distance arises. The procedure identifies that three additional compounds, BaBiK, CdPNa, and LaPtSb, should be included in the training process. These compounds are highlighted with red circles in Fig. 4, and Fig. 7 shows the distance in PC space after each iteration.

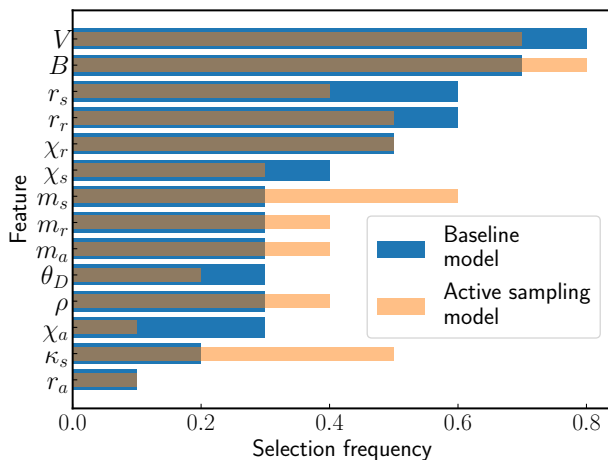


Fig. 5: Selection frequencies for the 14 features in the EFS using RF regression for the baseline (blue bars) and active sampling (orange bars) models.

4.2. Exhaustive feature selection analysis

Fig. 5 compares the EFS feature selection frequency of the baseline and active sampling ML models. The baseline and active sampling models use on average 5.7 and 5.9 features out of the 14 potential features, respectively. The relatively few features selected is in line with the recent results of Miyazaki et al. [60] finding that using a limited subset of features gives the best ML performance, which can be linked to the fact that redundant features can cause overfitting. In both the baseline and active sampling models, B and V are the most frequently selected features, in agreement with their high Spearman correlation with $\kappa_\ell^{\text{TDEP}}$.

There are some notable differences between the EFS for the active sampling model and the baseline model. In particular, the selection frequency of m_s increases from 0.3 to 0.6 for the active sampling model. This result reflects that the variation of masses in the primitive cell is linked to low lattice thermal conductivity, such as for BaBiK. The selection frequencies for κ_s and B also increase for the active sampling model.

Table 1: Performance metrics for predicting $\log(\kappa_\ell^{\text{TDEP}})$ for the 32 test compounds using the active sampling and baseline models. The metrics are: R2-score, root-mean-square error (RMSE), Spearman correlation, and Pearson correlation. The standard deviations are in parenthesis.

	Active	Baseline
R2	0.84 (0.03)	0.36 (0.13)
RMSE	0.21 (0.02)	0.43 (0.04)
Spearman	0.85 (0.04)	0.79 (0.07)
Pearson	0.93 (0.02)	0.64 (0.09)

4.3. Enhanced machine learning performance with active sampling

Fig. 6 (a) compares the predictions of the baseline model and the active sampling model on a logarithmic scale as used in the training. The error bars indicate the standard deviation of the predictions of the 10 models. The figure shows that the active sampling model has a superior ability to identify the compounds with low $\kappa_\ell^{\text{TDEP}}$. Predictions for the three compounds found with PCA, highlighted with red circles, are not provided for the active sampling model as they are included in the training sets of the model. Fig. 6 (b) shows the corresponding comparison with a linear scale, with compounds sorted according to $\kappa_\ell^{\text{TDEP}}$. In most of the cases, the active sampling model predictions, κ_ℓ^{AS} , are higher than $\kappa_\ell^{\text{TDEP}}$ for low $\kappa_\ell^{\text{TDEP}}$ compounds, and vice versa for high $\kappa_\ell^{\text{TDEP}}$ compounds. This is also seen in the logarithmic scale of Fig. 6 (a). Even if the numerical precision of the active sampling model for the compounds with low $\kappa_\ell^{\text{TDEP}}$ is quite modest, which can be linked to the limited sampling in this region of feature space, the model identifies the compounds with the lowest $\kappa_\ell^{\text{TDEP}}$. Appendix A: Table A.1 provides the numerical values of $\kappa_\ell^{\text{TDEP}}$ and κ_ℓ^{AS} at 500 K.

Table 1 summarizes various performance metrics of the ML models. The baseline model predictions, $\log(\kappa_\ell^{\text{BL}})$, has a Spearman correlation of 0.79 with $\log(\kappa_\ell^{\text{TDEP}})$, which is larger than the correlation of Carrete et al. [18] of 0.74. Their model is based on fewer training samples, but more complex features. However, even though the Spearman correlation metric is fair and the low $\kappa_\ell^{\text{TDEP}}$ compounds do tend

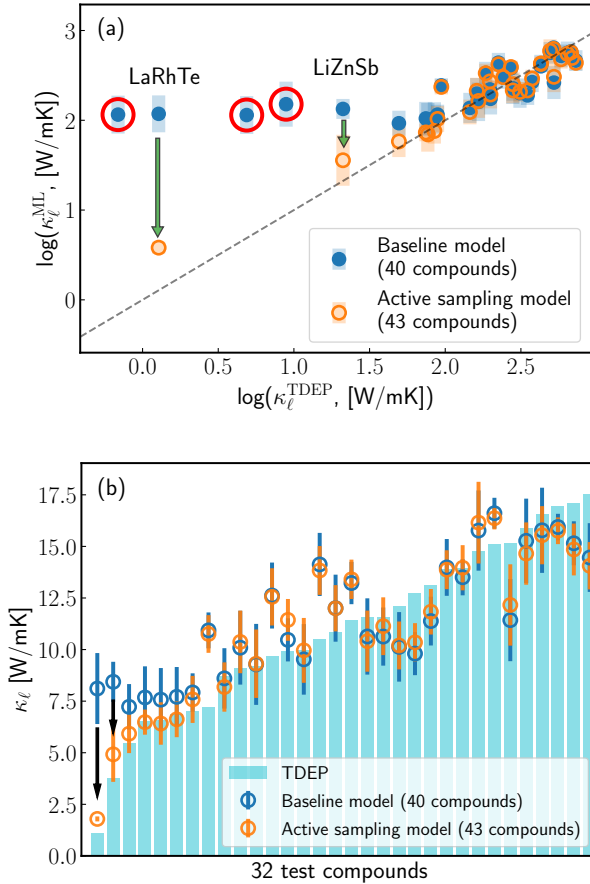


Fig. 6: a) Parity plot for predictions made on the test set. The horizontal axis shows $\log(\kappa_\ell^{\text{TDEP}})$ at 500 K, while the vertical axis shows the predictions. Blue (orange) circles indicate the predictions made by the baseline (active sampling) model. b) Corresponding comparison for $\kappa_\ell^{\text{TDEP}}$. The turquoise bars indicate $\kappa_\ell^{\text{TDEP}}$ at 500 K.

to be in the lower end of the spectrum of $\log(\kappa_\ell^{\text{BL}})$, the model fails to differentiate between the truly low $\kappa_\ell^{\text{TDEP}}$ compounds and the rest. The Spearman correlation of the active sampling model increases to 0.85. The superior ability of the active sampling model to predict properties of compounds with low $\kappa_\ell^{\text{TDEP}}$ results in improvement of the other performance metrics as well.

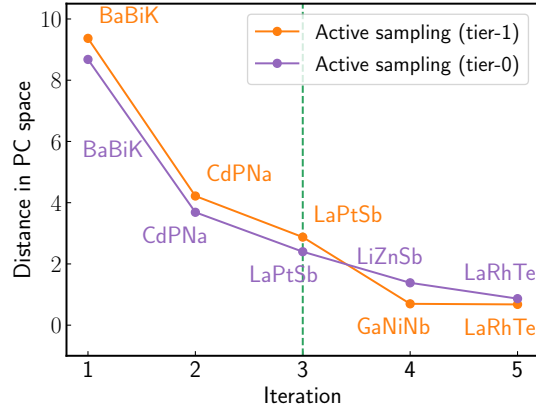


Fig. 7: Distance in PC space between the compound that is farthest from the training pool and its closest training pool neighbor after each iteration of sampling. Orange indicates PC space distance in the space spanned with tier-1 features, and purple shows the results for tier-0 features. The green line indicates the point at which we stop the inclusion of more compounds.

4.4. Machine learning at tier-0 level

The need for DFT-level input can be a drawback of using tier-1 features, as in some cases, experimental or calculated lattice constants are known while elastic tensors or bulk moduli are lacking. Thus, to uncover the potential of ML based on simpler features, we compare compound sampling and ML using tier-0 and tier-1 features. PCA-based active sampling with tier-0 features identifies the same three compounds as found earlier, as shown in Fig. 7 and Fig. 8 (a). We allow for LiZnSb to be in the test set in this case, even though the drop-off in PC distance is less steep, as it allows for direct comparison of ML performance when using tier-0 and tier-1 features.

Fig. 8 (b) compares the EFS selection frequencies of the active sampling models with tier-0 and tier-1 features. The average number of features chosen in the EFS for the active sampling model (tier-0) is 4.7, and increased selection frequencies are seen for χ_a and r_s .

Fig. 8 (c) shows that the active sampling model (tier-0) identifies the lowest $\kappa_\ell^{\text{TDEP}}$ compound, but fails to differentiate the second and third lowest from

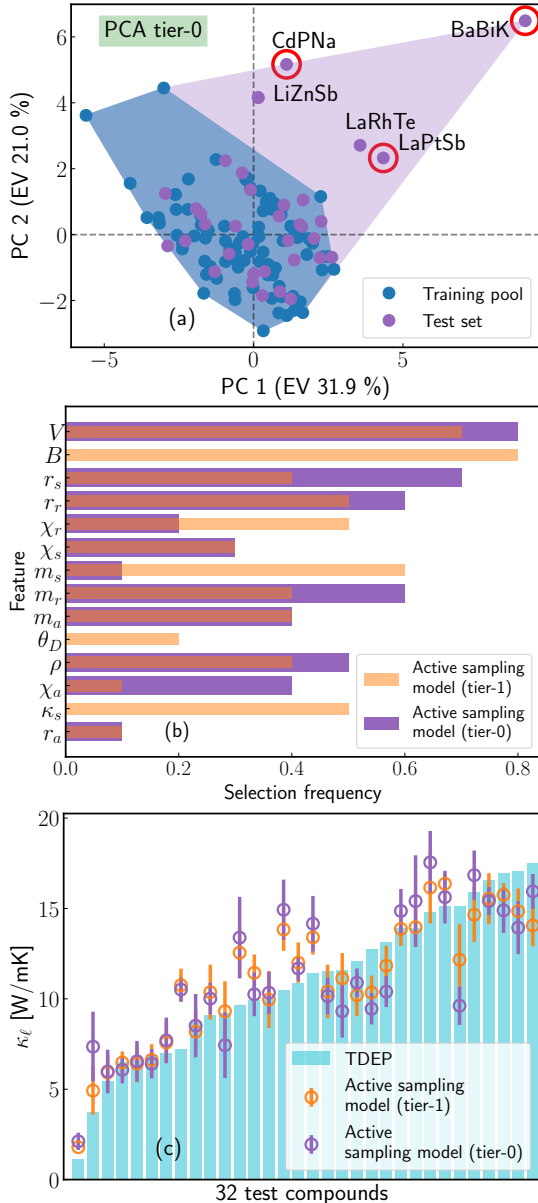


Fig. 8: (a) PCA plot for the compounds using tier-0 features. The horizontal axis shows the first PC while the vertical axis shows the second. (b) Selection frequencies from the EFS using RF regression for the active sampling models using tier-0 and tier-1 features. (c) Predicted and TDEP lattice thermal conductivity using active sampling models based on tier-0 and tier-1 features.

the rest. This model has weaker predictivity overall compared to the active sampling model (tier-1), with an R2-score of 0.73 and Spearman correlation of 0.78. Despite that tier-0 features are used, the active sampling model (tier-0) outperforms the baseline model, underlining the importance of sample selection.

We also note that pre-sampling using PCA with tier-0 features could be used for pruning the test set. This can be done by excluding compounds that lie close to or within already sampled compound clusters in PC space. This would reduce the number of compounds in the test set, and thus reduce the computational resources needed for calculating the tier-1 DFT features.

While the performance gain when using more complex features and larger training sets has been demonstrated in earlier studies [20–23, 60, 73–75], this work demonstrates that using rather modest training set sizes and low feature complexity can give reliable predictions by adopting active sample selection.

On a cautionary note, the use of semi-random selection rather than truly random selection accentuates the performance gains when doing active sampling. We also find that only including one or two of the low lattice thermal conductivity compounds in the models significantly reduces performance compared to including all three. Performance with a truly random model would hence be sensitive to exactly which training samples are selected. In any case, a key advantage of PCA is that when used in the process to include additional HH compounds, we have a procedure to identify whether the properties of a given compound can be predicted reliably.

4.5. Comparison with experiments

Computed and predicted lattice thermal conductivities do not always agree perfectly with that of experiments. For comparison, the $\kappa_{\ell}^{\text{TDEP}}$ for NbCoSn and ZrNiSn of 12.2 W/mK and 10.8 W/mK are higher than lattice thermal conductivity measured in experiments: 7.0 W/mK [76] and 8.7 W/mK [77] for NbCoSn; 5.4 W/mK [78] and 6.1 W/mK [79] for ZrNiSn. Predictions made by the active sampling model (tier-1) for NbCoSn and ZrNiSn are 13.4 W/mK and 12.0 W/mK, respectively, when trained on calculated data. At the current level of theory,

the difference between the ML predictions and TDEP lattice thermal conductivity is therefore much lower than that of experiment and theory. Sample dependent phonon scattering mechanisms due to physical properties such as grain boundaries, intrinsic disorder, and antisite defects can drastically reduce lattice thermal conductivity [79–85], and can explain why experimentally measured lattice thermal conductivity is lower than predictions when computed lattice thermal conductivity only includes three-phonon and isotope scattering. Including such scattering mechanisms in the calculated lattice thermal conductivity can give values closer to that of experiment [81, 86], which future studies should contemplate including in ML training for making models more representative of the lattice thermal conductivity of real-world samples.

5. Summary and conclusion

This study has explored strategies for using machine learning for finding low lattice thermal conductivity compounds using a limited number of training samples. Moreover, rather simple features were used, which can be found directly in material databases or computed straightforwardly. The exploration was made possible by computing lattice thermal conductivity with the temperature-dependent effective potential method for 122 half-Heusler compounds. We first demonstrated how a model based on a semi-random pool of materials (i.e. assumed "bad luck" in the training set) was unable to separate the truly low lattice thermal conductivity compounds in the test set from the rest. To improve the model, we used active sample selection based on principal component analysis. This approach suggested three compounds to be included in the training process. The subsequent inclusions resulted in a substantial improvement of model performance, in particular the ability to identify the remaining low lattice thermal conductivity compounds in the test set. Active sample selection without density functional theory-based features also identified necessary compounds to include in the model, but excluding the features in the model training resulted in weaker predictivity.

Our study demonstrates how active sampling can improve machine learning predictivity by accurately predicting properties of compounds dissimilar from the typical ones in a material class. More narrowly, we expect the procedure outlined here to be adopted to study broader classes of materials to systematically identify new low lattice thermal conductivity compounds.

6. Data availability

The data forming the basis of this study is available from the authors upon reasonable request.

Acknowledgements

The computations in this work were done on the high performance cluster Saga managed by UNINETT Sigma2. This work is part of the Allotherm project (Project No. 314778) supported by the Research Council of Norway. We further thank Øven Andreas Grimenes for helpful discussion and proofreading.

Appendix A.

Table A.1 shows $\kappa_{\ell}^{\text{TDEP}}$ for the HH compounds. Predictions made with the active sampling model (tier-1) are in the parenthesis.

References

- [1] G. J. Snyder, E. S. Toberer, Complex thermoelectric materials, *Nat. Mater.* 7 (2) (2008) 105–114. doi:10.1038/nmat2090.
- [2] D. Champier, Thermoelectric generators: A review of applications, *Energy Convers. Manag.* 140 (2017) 167–181. doi:10.1016/j.enconman.2017.02.070.
- [3] J. J. G. Moreno, A review of recent progress in thermoelectric materials through computational methods, *Mater. Renew. Sustain. Energy* (2020) 22doi:10.1007/s40243-020-00175-5.

- [4] J. Wei, L. Yang, Z. Ma, P. Song, M. Zhang, J. Ma, F. Yang, X. Wang, Review of current high-ZT thermoelectric materials, *J Mater Sci* 55 (27) (2020) 12642–12704. doi:10.1007/s10853-020-04949-0.
- [5] J. Recatala-Gomez, A. Suwardi, I. Nandhakumar, A. Abutaha, K. Hippalgaonkar, Toward accelerated thermoelectric materials and process discovery, *ACS Appl. Energy Mater.* 3 (3) (2020) 2240–2257. doi:10.1021/acsaem.9b02222.
- [6] P. P. Paskov, M. Slomski, J. H. Leach, J. F. Muth, T. Paskova, Effect of Si doping on the thermal conductivity of bulk GaN at elevated temperatures – theory and experiment, *AIP Advances* 7 (9) (2017) 095302. doi:10.1063/1.4989626.
- [7] S. Y. Kim, H.-S. Kim, K. H. Lee, H.-j. Cho, S.-s. Choo, S.-w. Hong, Y. Oh, Y. Yang, K. Lee, J.-H. Lim, S.-M. Choi, H. J. Park, W. H. Shin, S.-i. Kim, Influence of Pd doping on electrical and thermal properties of n-type $\text{Cu}_{0.008}\text{Bi}_2\text{Te}_{2.7}\text{Se}_{0.3}$ alloys, *Materials* 12 (24) (2019) 4080. doi:10.3390/ma12244080.
- [8] K. Berland, N. Shulumba, O. Hellman, C. Persson, O. M. Løvvik, Thermoelectric transport trends in group 4 half-Heusler alloys, *J. Appl. Phys.* 126 (14) (2019) 145102. arXiv:https://doi.org/10.1063/1.5117288.
- [9] R. Li, X. Li, L. Xi, J. Yang, D. J. Singh, W. Zhang, High-throughput screening for advanced thermoelectric materials: diamond-like ABX_2 compounds, *ACS Appl. Mater. Interfaces* 11 (28) (2019) 24859–24866. doi:10.1021/acsaem.9b01196.
- [10] K. Choudhary, K. F. Garrity, F. Tavazza, Data-driven discovery of 3D and 2D thermoelectric materials, *J. Condens. Matter Phys.* 32 (47) (2020) 475501. doi:10.1088/1361-648X/aba06b.
- [11] J. Liu, S. Han, G. Cao, Z. Zhou, C. Sheng, H. Liu, A high-throughput descriptor for prediction of lattice thermal conductivity of half-Heusler compounds, *J. Phys. D: Appl. Phys.* 53 (31) (2020) 315301. doi:10.1088/1361-6463/ab898e.
- [12] J. He, M. Amsler, Y. Xia, S. S. Naghavi, V. I. Hegde, S. Hao, S. Goedecker, V. Ozoliņš, C. Wolverton, Ultralow thermal conductivity in full Heusler semiconductors, *Phys. Rev. Lett.* 117 (4) (2016) 046602. doi:10.1103/PhysRevLett.117.046602.
- [13] P. R. Raghuvanshi, S. Mondal, A. Bhattacharya, A high throughput search for efficient thermoelectric half-Heusler compounds, *J. Mater. Chem. A* 8 (47) (2020) 25187–25197. doi:10.1039/D0TA06810A.
- [14] T.-T. Jia, Z. Feng, S. Guo, X. Zhang, Y. Zhang, Screening promising thermoelectric materials in binary chalcogenides through high-throughput computations, *ACS Appl. Mater. Interfaces* 12 (2020) 11852–11864. doi:10.1021/acsaem.9b23297.
- [15] A. Togo, L. Chaput, I. Tanaka, Distributions of phonon lifetimes in Brillouin zones, *Phys. Rev. B* 91 (9) (2015) 094306. doi:10.1103/PhysRevB.91.094306.
- [16] O. Hellman, I. A. Abrikosov, Temperature-dependent effective third-order interatomic force constants from first principles, *Phys. Rev. B* 88 (14) (2013) 144301. doi:10.1103/PhysRevB.88.144301.
- [17] F. Zhou, W. Nielson, Y. Xia, V. Ozoliņš, Lattice anharmonicity and thermal conductivity from compressive sensing of first-principles calculations, *Phys. Rev. Lett.* 113 (18) (2014) 185501. doi:10.1103/PhysRevLett.113.185501.
- [18] J. Carrete, W. Li, N. Mingo, S. Wang, S. Curtarolo, Finding unprecedentedly low-thermal-conductivity half-Heusler semiconductors via high-throughput materials modeling, *Phys. Rev. X* 4 (1) (2014) 011019. doi:10.1103/PhysRevX.4.011019.

- [19] S. Ju, R. Yoshida, C. Liu, K. Hongo, T. Tadano, Exploring diamond-like lattice thermal conductivity crystals via feature-based transfer learning (2019) 27doi:10.1103/PhysRevMaterials.5.053801.
- [20] L. Chen, H. Tran, R. Batra, C. Kim, R. Ramprasad, Machine learning models for the lattice thermal conductivity prediction of inorganic materials, *Comput. Mater. Sci.* 170 (2019) 109155. doi:10.1016/j.commatsci.2019.109155.
- [21] X. Wang, S. Zeng, Z. Wang, J. Ni, Identification of crystalline materials with ultra-low thermal conductivity based on machine learning study, *J. Phys. Chem. C* 124 (16) (2020) 8488–8495. doi:10.1021/acs.jpcc.9b11610.
- [22] C. Loftis, K. Yuan, Y. Zhao, M. Hu, J. Hu, Lattice thermal conductivity prediction using symbolic regression and machine learning, *J. Phys. Chem. A* 125 (1) (2021) 435–450. doi:10.1021/acs.jpca.0c08103.
- [23] T. Zhu, R. He, S. Gong, T. Xie, P. Gorai, K. Nielsch, J. C. Grossman, Charting lattice thermal conductivity for inorganic crystals and discovering rare earth chalcogenides for thermoelectrics, *Energy Environ. Sci.* 14 (2021) 3559–3566. doi:10.1039/D1EE00442E.
- [24] D. Visaria, A. Jain, Machine-learning-assisted space-transformation accelerates discovery of high thermal conductivity alloys, *Appl. Phys. Lett.* 117 (20) (2020) 202107. doi:10.1063/5.0028241.
- [25] C. M. Collins, L. M. Daniels, Q. Gibson, M. W. Gaultois, M. Moran, R. Feetham, M. J. Pitcher, M. S. Dyer, C. Delacotte, M. Zanella, C. A. Murray, G. Glodan, O. Pérez, D. Pelloquin, T. D. Manning, J. Alaria, G. R. Darling, J. B. Claridge, M. J. Rosseinsky, Discovery of a low thermal conductivity oxide guided by probe structure prediction and machine learning, *Angew. Chem. Int. Ed* (2021). doi:https://doi.org/10.1002/anie.202102073.
- [26] M. W. Gaultois, A. O. Oliynyk, A. Mar, T. D. Sparks, G. J. Mulholland, B. Meredig, A recommendation engine for suggesting unexpected thermoelectric chemistries, *APL Mater.* 4 (5) (2016) 053213, arXiv: 1502.07635. doi:10.1063/1.4952607.
- [27] F. Casper, T. Graf, S. Chadov, B. Balke, C. Felser, Half-Heusler compounds: novel materials for energy and spintronic applications, *Semicond. Sci. Technol.* 27 (6) (2012) 063001. doi:10.1088/0268-1242/27/6/063001.
- [28] J.-W. G. Bos, R. A. Downie, Half-Heusler thermoelectrics: a complex class of materials, *J. Condens. Matter Phys.* 26 (43) (2014) 433201. doi:10.1088/0953-8984/26/43/433201.
- [29] T. Zhu, C. Fu, H. Xie, Y. Liu, X. Zhao, High efficiency half-Heusler thermoelectric materials for energy harvesting, *Adv. Energy Mater.* 5 (19) (2015) 1500588. doi:10.1002/aenm.201500588.
- [30] B. Yuan, B. Wang, L. Huang, X. Lei, L. Zhao, C. Wang, Q. Zhang, Effects of Sb substitution by Sn on the thermoelectric properties of Zr-CoSb, *J. Electron. Mater.* 46 (5) (2017) 3076–3082. doi:10.1007/s11664-016-5168-z.
- [31] A. Hori, S. Minami, M. Saito, F. Ishii, First-principles calculation of lattice thermal conductivity and thermoelectric figure of merit in ferromagnetic half-Heusler alloy CoMnSb, *Appl. Phys. Lett.* 116 (24) (2020) 242408. doi:10.1063/1.5143038.
- [32] N. S. Chauhan, P. R. Raghuvanshi, K. Tyagi, K. K. Johari, L. Tyagi, B. Gahtori, S. Bathula, A. Bhattacharya, S. D. Mahanti, V. N. Singh, Y. V. Kolen'ko, A. Dhar, Defect engineering for enhancement of thermoelectric performance of (Zr, Hf)NiSn-Based n-type half-Heusler alloys, *J. Phys. Chem. C* 124 (16) (2020) 8584–8593. doi:10.1021/acs.jpcc.0c00681.
- [33] H. Zhu, J. Mao, Y. Li, J. Sun, Y. Wang, Q. Zhu, G. Li, Q. Song, J. Zhou, Y. Fu, R. He, T. Tong, Z. Liu, W. Ren, L. You, Z. Wang,

- J. Luo, A. Sotnikov, J. Bao, K. Nielsch, G. Chen, D. J. Singh, Z. Ren, Discovery of TaFeSb-based half-Heuslers with high thermoelectric performance, *Nat. Commun.* 10 (1) (2019) 270. doi:10.1038/s41467-018-08223-5.
- [34] H.-L. Sun, C.-L. Yang, M.-S. Wang, X.-G. Ma, Remarkably high thermoelectric efficiencies of the half-Heusler compounds BXGa (X = Be, Mg, and Ca), *ACS Appl. Mater. Interfaces* 12 (5) (2020) 5838–5846. doi:10.1021/acsami.9b19198.
- [35] D. Zhao, M. Zuo, Z. Wang, X. Teng, H. Geng, Synthesis and thermoelectric properties of tantalum-doped ZrNiSn half-Heusler alloys, *Funct. Mater. Lett.* 07 (03) (2014) 1450032. doi:10.1142/S1793604714500325.
- [36] J. Zhou, H. Zhu, T.-H. Liu, Q. Song, R. He, J. Mao, Z. Liu, W. Ren, B. Liao, D. J. Singh, Z. Ren, G. Chen, Large thermoelectric power factor from crystal symmetry-protected non-bonding orbital in half-Heuslers, *Nat. Commun.* 9 (2018). doi:10.1038/s41467-018-03866-w.
- [37] Z. Feng, Y. Fu, Y. Zhang, D. J. Singh, Characterization of rattling in relation to thermal conductivity: ordered half-Heusler semiconductors, *Phys. Rev. B* 101 (6) (2020) 064301, arXiv:2001.08029. doi:10.1103/PhysRevB.101.064301.
- [38] Q. Y. Xue, H. J. Liu, D. D. Fan, L. Cheng, B. Y. Zhao, J. Shi, LaPtSb: a half-Heusler compound with high thermoelectric performance, *Phys. Chem. Chem. Phys.* 18 (27) (2016) 17912–17916. doi:10.1039/C6CP03211G.
- [39] S. H. Han, Z. Z. Zhou, C. Y. Sheng, J. H. Liu, L. Wang, H. M. Yuan, H. J. Liu, High thermoelectric performance of half-Heusler compound BiBaK with intrinsically low lattice thermal conductivity, *J. Condens. Matter Phys.* 32 (42) (2020) 425704. doi:10.1088/1361-648X/aba2e7.
- [40] G. Samsonidze, B. Kozinsky, Accelerated screening of thermoelectric materials by first-principles computations of electron-phonon scattering, *Adv. Energy Mater.* 8 (20) (2018) 1800246. doi:10.1002/aenm.201800246.
- [41] S. Zhang, B. Xu, Y. Lin, C. Nan, W. Liu, First-principles study of the layered thermoelectric material TiNBr, *RSC Adv.* 9 (23) (2019) 12886–12894. doi:10.1039/C9RA00247B.
- [42] D. Sarkar, T. Ghosh, S. Roychowdhury, R. Arora, S. Sajan, G. Sheet, U. V. Waghmare, K. Biswas, Ferroelectric instability induced ultralow thermal conductivity and high thermoelectric performance in rhombohedral *p*-Type GeSe crystal, *J. Am. Chem. Soc.* 142 (28) (2020) 12237–12244. doi:10.1021/jacs.0c03696.
- [43] L.-D. Zhao, S.-H. Lo, Y. Zhang, H. Sun, G. Tan, C. Uher, C. Wolverton, V. P. Dravid, M. G. Kanatzidis, Ultralow thermal conductivity and high thermoelectric figure of merit in SnSe crystals, *Nature* 508 (7496) (2014) 373–377. doi:10.1038/nature13184.
- [44] G. Kresse, J. Hafner, *Ab initio* molecular dynamics for liquid metals, *Phys. Rev. B* 47 (1) (1993) 558–561. doi:10.1103/PhysRevB.47.558.
- [45] G. Kresse, J. Furthmüller, Efficiency of *ab initio* total energy calculations for metals and semiconductors using a plane-wave basis set, *Comput. Mater. Sci.* 6 (1) (1996) 15–50. doi:10.1016/0927-0256(96)00008-0.
- [46] G. Kresse, J. Furthmüller, Efficient iterative schemes for *ab initio* total-energy calculations using a plane-wave basis set, *Phys. Rev. B* 54 (16) (1996) 11169–11186. doi:10.1103/PhysRevB.54.11169.
- [47] J. P. Perdew, A. Ruzsinszky, G. I. Csonka, O. A. Vydrov, G. E. Scuseria, L. A. Constantin, X. Zhou, K. Burke, Restoring the density-gradient expansion for exchange in solids and surfaces, *Phys. Rev. Lett.* 100 (13) (2008) 136406. doi:10.1103/PhysRevLett.100.136406.
- [48] G. I. Csonka, J. P. Perdew, A. Ruzsinszky, P. H. T. Philipsen, S. Lebègue, J. Paier, O. A. Vydrov, J. G. Ángyán, Assessing the performance of recent density functionals for bulk solids, *Phys. Rev. B* 79 (15) (2009) 155107. doi:10.1103/PhysRevB.79.155107.

- [49] O. Hellman, I. A. Abrikosov, S. I. Simak, Lattice dynamics of anharmonic solids from first principles, *Phys. Rev. B* 84 (18) (2011) 180301. doi:10.1103/PhysRevB.84.180301.
- [50] S.-i. Tamura, Isotope scattering of dispersive phonons in Ge, *Phys. Rev. B* 27 (2) (1983) 858–866. doi:10.1103/PhysRevB.27.858.
- [51] S.-i. Tamura, Isotope scattering of large-wave-vector phonons in GaAs and InSb: Deformation-dipole and overlap-shell models, *Phys. Rev. B* 30 (2) (1984) 849–854. doi:10.1103/PhysRevB.30.849.
- [52] N. Shulumba, O. Hellman, A. J. Minnich, Intrinsic localized mode and low thermal conductivity of PbSe, *Phys. Rev. B* 95 (2017) 014302. doi:10.1103/PhysRevB.95.014302.
- [53] O. Anderson, A simplified method for calculating the debye temperature from elastic constants, *J Phys Chem Solids* 24 (7) (1963) 909–917. doi:10.1016/0022-3697(63)90067-2.
- [54] L. Breiman, Random forests, *Mach. Learn.* 45 (1) (2001) 5–32. doi:10.1023/A:1010933404324.
- [55] S. Raschka, V. Mirjalili, Python machine learning: machine learning and deep learning with Python, Scikit-Learn, and TensorFlow, 2nd Edition, 2nd Edition, Packt Publishing, 2017.
- [56] H. K. Jabbar, R. Z. Khan, Methods to avoid over-fitting and under-fitting in supervised machine learning (comparative study), in: *Computer Science, Communication and Instrumentation Devices*, Research Publishing Services, 2014, pp. 163–172. doi:10.3850/978-981-09-5247-1_017.
- [57] S. Raschka, MLxtend: Providing machine learning and data science utilities and extensions to Python’s scientific computing stack, *JOSS* 3 (24) (2018) 638. doi:10.21105/joss.00638.
- [58] F. Pedregosa, G. Varoquaux, A. Gramfort, V. Michel, B. Thirion, O. Grisel, M. Blondel, P. Prettenhofer, R. Weiss, V. Dubourg, J. Vanderplas, A. Passos, D. Cournapeau, Scikit-learn: machine learning in Python, *J. Mach. Learn. Res.* 12 (2011) 2825.
- [59] O. Tomic, T. Graff, K. Liland, T. Næs, Hoggorm: a python library for explorative multivariate statistics, *JOSS* 4 (39) (2019) 980. doi:10.21105/joss.00980.
- [60] H. Miyazaki, T. Tamura, M. Mikami, K. Watanabe, N. Ide, O. M. Ozkendir, N. Toichi, Machine learning based prediction of lattice thermal conductivity for half-Heusler compounds using atomic information, *Sci. Rep.* (2021). doi:10.1038/s41598-021-92030-4.
- [61] H. Liang, V. Stanev, A. G. Kusne, I. Takeuchi, CRYSPNet: Crystal structure predictions via neural networks, *Phys. Rev. Mater.* 4 (2020) 123802. doi:10.1103/PhysRevMaterials.4.123802.
- [62] Y. Li, W. Yang, R. Dong, J. Hu, MLaticeABC: Generic lattice constant prediction of crystal materials using machine learning, *ACS Omega* 6 (2021) 11585 – 11594. doi:10.1021/acsomega.1c00781.
- [63] J. Meija, T. Coplen, M. Berglund, W. Brand, P. De Bièvre, M. Gröning, N. Holden, J. Irrgeher, R. Loss, T. Walczyk, T. Prohaska, Atomic weights of the elements 2013 (iupac technical report), *Pure Appl. Chem.* 88 (2016) 265–291. doi:10.1515/pac-2015-0305.
- [64] L. C. Allen, Electronegativity is the average one-electron energy of the valence-shell electrons in ground-state free atoms, *J. Am. Chem. Soc.* 111 (1989) 9003–9014. doi:10.1021/JA00207A003.
- [65] B. Cordero, V. Gómez, A. Platero-Prats, M. Revés, J. Echeverría, E. Cremades, F. Barragán, S. Alvarez, Covalent radii revisited, *Dalton trans.* 21 (2008) 2832–8. doi:10.1039/b801115j.
- [66] G. A. Slack, Nonmetallic crystals with high thermal conductivity, *J Phys Chem Solids* 34 (2) (1973) 15. doi:10.1016/0022-3697(73)90092-9.

- [67] T. Jia, G. Chen, Y. Zhang, Lattice thermal conductivity evaluated using elastic properties, *Phys. Rev. B* 95 (15) (2017) 155206. doi:10.1103/PhysRevB.95.155206.
- [68] S. Ju, J. Shiomi, Materials informatics for heat transfer: recent progresses and perspectives, *Nanoscale Microscale Thermophys. Eng.* 23 (2) (2019) 157–172. doi:10.1080/15567265.2019.1576816.
- [69] A. Jain, S. P. Ong, G. Hautier, W. Chen, W. D. Richards, S. Dacek, S. Cholia, D. Gunter, D. Skinner, G. Ceder, K. A. Persson, Commentary: The Materials Project: A materials genome approach to accelerating materials innovation, *APL Mater.* 1 (1) (2013) 011002. doi:10.1063/1.4812323.
- [70] R. Gautier, X. Zhang, L. Hu, L. Yu, Y. Lin, T. O. L. Sunde, D. Chon, K. R. Poeppelmeier, A. Zunger, Prediction and accelerated laboratory discovery of previously unknown 18-electron ABX compounds, *Nature Chem* 7 (4) (2015) 308–316. doi:10.1038/nchem.2207.
- [71] M. W. Gaultois, T. D. Sparks, How much improvement in thermoelectric performance can come from reducing thermal conductivity?, *Appl. Phys. Lett.* 104 (11) (2014) 113906. doi:10.1063/1.4869232.
- [72] J. An, A. Subedi, D. Singh, Ab initio phonon dispersions for PbTe, *Solid State Commun.* 148 (9-10) (2008) 417–419. doi:10.1016/j.ssc.2008.09.027.
- [73] R. Juneja, G. Yumnam, S. Satsangi, A. K. Singh, Coupling the high-throughput property map to machine learning for predicting lattice thermal conductivity, *Chem. Mater.* 31 (14) (2019) 5145–5151. doi:10.1021/acs.chemmater.9b01046.
- [74] R. Juneja, A. K. Singh, Guided patchwork kriging to develop highly transferable thermal conductivity prediction models, *J. Phys. Mater.* 3 (2) (2020) 024006. doi:10.1088/2515-7639/ab78f2.
- [75] A. Tewari, S. Dixit, N. Sahni, S. P. Bordas, Machine learning approaches to identify and design low thermal conductivity oxides for thermoelectric applications, *DCE* 1 (2020) e8. doi:10.1017/dce.2020.7.
- [76] R. He, L. Huang, Y. Wang, G. Samsonidze, B. Kozinsky, Q. Zhang, Z. Ren, Enhanced thermoelectric properties of n-type NbCoSn half-Heusler by improving phase purity, *APL Mater.* 4 (2016) 104804. doi:10.1063/1.4952994.
- [77] R. Yan, W. Xie, B. Balke, G. Chen, A. Weidenkaff, Realizing p-type NbCoSn half-Heusler compounds with enhanced thermoelectric performance via Sc substitution, *Sci. Technol. Adv. Mater.* 21 (2020). doi:10.1080/14686996.2020.1726715.
- [78] A. Bahrami, P. Ying, U. Wolff, N. P. Rodríguez, G. Schierning, K. Nielsch, R. He, Reduced lattice thermal conductivity for half-Heusler Zr-NiSn through cryogenic mechanical alloying, *ACS Appl. Mater. Interfaces* 13 (32) (2021) 38561–38568. doi:10.1021/acsami.1c05639.
- [79] H. Xie, H. Wang, C. Fu, Y. Liu, G. Snyder, X. Zhao, T. Zhu, The intrinsic disorder related alloy scattering in ZrNiSn half-Heusler thermoelectric materials, *Sci. Rep.* 4 (2014) 6888. doi:10.1038/srep06888.
- [80] M. Schrade, K. Berland, S. Eliassen, M. Guzik, C. Echevarria-Bonet, M. Sørby, P. Jenus, B. Hauback, R. Tofan, A. Gunnæs, C. Persson, O. Løvvik, T. Finstad, The role of grain boundary scattering in reducing the thermal conductivity of polycrystalline XNiSn (X = Hf, Zr, Ti) half-Heusler alloys, *Sci. Rep.* 7 (2017). doi:10.1038/s41598-017-14013-8.
- [81] S. N. H. Eliassen, A. Katre, G. K. H. Madsen, C. Persson, O. M. Løvvik, K. Berland, Lattice thermal conductivity of $Ti_xZr_yHf_{1-x-y}NiSn$ half-Heusler alloys calculated from first principles: Key role of nature of phonon modes, *Phys. Rev. B* 95 (2017) 045202. doi:10.1103/PhysRevB.95.045202.

- [82] A. Katre, J. Carrete, N. Mingo, Unraveling the dominant phonon scattering mechanism in thermoelectric compound ZrNiSn, *J. Mater. Chem. A* 4 (07 2016). doi:10.1039/C6TA05868J.
- [83] J. Carrete Montaña, N. Mingo, S. Wang, S. Curtarolo, Nanograined half-Heusler semiconductors as advanced thermoelectrics: An ab initio high-throughput statistical study, *Adv. Funct. Mater.* 24 (2014). doi:10.1002/adfm.201401201.
- [84] H. Hazama, M. Matsubara, R. Asahi, T. Takeuchi, Improvement of thermoelectric properties for half-Heusler TiNiSn by interstitial Ni defects, *J. Appl. Phys.* 110 (2011). doi:10.1063/1.3633518.
- [85] H. Miyazaki, O. M. Ozkendir, S. Günaydın, K. Watanabe, K. Soda, Y. Nishino, Probing local distortion around structural defects in half-Heusler thermoelectric NiZrSn alloy, *Sci. Rep.* 10 (2020) 19820. doi:10.1038/s41598-020-76554-9.
- [86] H. Geng, X. Meng, H. Zhang, J. Zhang, Lattice thermal conductivity of nanograined half-Heusler solid solutions, *Appl. Phys. Lett.* 104 (20) (2014) 202104. doi:10.1063/1.4879248.

Table A.1: Calculated $\kappa_\ell^{\text{TDEP}}$ at 500 K for the HHs. The 32 compounds in the final test set are highlighted with bold text, and predictions made with the active sampling model (tier-1) are in parenthesis.

κ_ℓ [W/mK]	κ_ℓ [W/mK]	κ_ℓ [W/mK]	κ_ℓ [W/mK]
LaPtSb 0.85	ZrPtGe 8.27	ZrCoBi 11.54 (10.41)	TaCoGe 15.47
LaRhTe 1.11 (1.79)	TiPdSn 8.42	NbIrSn 11.57 (11.13)	VRuAs 15.52
BaBiK 1.99	NbRuBi 8.70 (8.18)	HfCoAs 11.64	TiPdGe 15.78
CdPNa 2.58	TiPtSn 8.88	TiRhSb 11.72	GaNiNb 15.88 (14.65)
LiZnSb 3.76 (4.92)	HfIrAs 9.04	HfRhAs 11.76	NbOsAs 15.95
TaIrPb 5.20	ZrNiPb 9.10 (10.37)	TaIrSn 11.84	SiCoTa 16.28
TiPtPb 5.43	VOsSb 9.12	NbOsSb 11.86	VRhGe 16.57 (15.54)
BiPdSc 5.44 (5.92)	AlSiLi 9.18	ZrRhSb 11.89	VCoGe 16.58
BiNiY 5.46	ZrPtSn 9.20 (9.32)	HfCoBi 12.11 (10.20)	TaRuAs 16.60
HfPtPb 5.48	HfPdSn 9.32	NbCoSn 12.23	GaPtTa 16.75
HfPdPb 5.86	VRuSb 9.32	TaFeBi 12.40	VOsAs 16.82
TaOsBi 5.90	ZrPdSn 9.37	HfCoSb 12.48	TaRhGe 16.85
TiPdPb 5.94	AsNiSc 9.46	ZrNiGe 12.48	VIrGe 16.95 (15.76)
TaRhPb 5.95	TaCoPb 9.66 (12.55)	NbRuSb 12.52	GeFeW 17.07
NbIrPb 6.07	NbRhSn 9.92 (11.44)	TiIrSb 12.73 (10.35)	TaFeSb 17.10 (14.85)
ZrPtPb 6.50 (6.48)	NbCoPb 9.95	TaRuSb 13.12 (11.83)	AlAuHf 17.11
HfIrBi 6.58	HfNiPb 9.96 (9.96)	TaCoSn 13.38	NbIrGe 17.21
ZrPdPb 6.59 (6.42)	HfPtSn 9.98	VFeSb 13.40	TiRhAs 17.52 (14.06)
TiIrBi 6.68	HfPdGe 10.28	HfIrSb 13.65	TaOsAs 18.09
ZrIrBi 6.88 (6.62)	TiNiSn 10.50 (13.83)	TeFeTi 13.82	TiCoBi 19.10
BiNiSc 6.97	ZrNiSn 10.84 (12.00)	TiCoSb 13.90 (13.87)	NbCoGe 19.37
HfRhBi 7.00	ZrIrSb 10.97	TiNiPb 13.91	TaIrGe 19.57
VIrSn 7.01	ZrPdGe 10.98	ZrCoAs 13.91 (13.97)	TiCoAs 19.92
TaRuBi 7.02 (7.58)	HfPtGe 11.08	TiIrAs 14.12	NbRuAs 20.21
VRhSn 7.11	TeRuZr 11.11	ZrCoSb 14.29	NbCoSi 20.31
ZrIrAs 7.20 (10.76)	HfNiSn 11.29	TiPtGe 14.34	NbRhGe 20.63
NbRhPb 7.21	VCoSn 11.30	ZrRhAs 14.54	NbFeAs 22.20
NbOsBi 7.26	TaRhSn 11.37	TiNiGe 14.78 (16.15)	VFeAs 22.60
ZrRhBi 7.33	NbFeBi 11.40	NbFeSb 15.00	LiBSi 23.45
AlGeLi 7.68	HfNiGe 11.41 (13.41)	TaFeAs 15.12 (16.37)	
TiRhBi 7.85	HfRhSb 11.49	TaOsSb 15.16 (12.16)	